Journal of Polymers and the Environment (2022) 30:5173–5189
https://doi.org/10.1007/s10924-022-02549-4

ORIGINAL PAPER

Designing PolyHIPE/CNC Nanocomposites for Application of Environmental Adsorption Processes

Ali Eslek[1] · Meltem Sözbir[1] · Hatice Hande Mert[2] · Mohammad Reza Moghbeli[3] · Yasaman Farahat[3] · Emine Hilal Mert[4]

Accepted: 1 August 2022 / Published online: 21 September 2022

Abstract

Cellulose nanocrystals (CNCs) are attracting specific interest in polymer nanocomposite preparation due to their contribution on physical and thermal properties, biocompatibility, and being a renewable feedstock. Surface modified CNCs have also remarkable potential in Pickering-emulsion preparation besides to developing of efficient adsorbent materials. In this work, polyHIPE/CNC nanocomposites from surface-modified CNC stabilized Pickering-HIPEs were designed and the Nile blue removal efficiency of CNC-based adsorbent from aqueous environment was reported. Surface modification of CNCs was achieved via grafting epoxy-terminated PEG on silylated CNCs. Highly stable Pickering-HIPEs were prepared according to experimental design matrix created based on varying four experimental parameters including nanoparticle loading, emulsifier amount, internal phase ratio, and stirring rate, for three distinctive levels. The main and interaction effects of experimental parameters on morphological and mechanical properties were expressed by mathematical model equations using statistical analysis. By using model equations, a polyHIPE/CNC nanocomposite was selected as adsorbent material, considering the main and interaction contribution of nanoparticle loading on cavity size, interconnected pore size, and specific surface area. The proposed adsorbent was tested in the adsorption of Nile blue from aqueous solutions and 87% of sorption efficiency was achieved. Moreover, kinetic mechanism of Nile blue adsorption was investigated and Freundlich isotherm was found to be as best fitted model consistent with pseudo second-order kinetic model. The designed polyHIPE/CNC nanocomposites have remarkable potential as efficient adsorbents which could be motivated for development of new CNC-based nanocomposites removal of different contaminants from wastewater.

Keywords Crystalline nanocellulose · Dicyclopentadiene · polyHIPE · Experimental design technique · Statistical analysis

Introduction

High internal phase emulsion (HIPE) templating is an alternative method used for the synthesis of open-cellular macroporous polymers with a well-defined morphology. The basis of the method relies on the usage of HIPEs as templates for the creation of porosity [1]. HIPEs are concentrated emulsions where the volume fraction of the dispersed phase is usually greater than 74.05% and the continuous phase has a minor fraction [2]. When the continuous phase is prepared to consist of polymerizable units, polymerization of the continuous phase and extraction of dispersed phase leads macroporous polymer foams. These foams are known as polyHIPEs [1, 3]. Macroporous polyHIPEs and their nanocomposites have different potential applications for preparing ion-exchange membranes, separation columns, catalyst supports, sensors, controlled drug delivery systems

✉ Hatice Hande Mert
hndmert@yalova.edu.tr

✉ Emine Hilal Mert
hmert@yalova.edu.tr

[1] Department of Polymer Materials Engineering, Institute of Graduate Studies, Yalova University, 77200 Yalova, Turkey

[2] Department of Chemical Engineering, Faculty of Engineering, Yalova University, 77200 Yalova, Turkey

[3] Smart Polymers and Nanocomposites Research Lab, School of Chemical Engineering, Iran University of Science and Technology, Tehran 16846–13114, Iran

[4] Department of Polymer Materials Engineering, Faculty of Engineering, Yalova University, 77200 Yalova, Turkey

[4, 5]. Although wastewater treatment can be achieved with different materials, such as composite photocatalysts based on photocatalytic degradation, as reported in the literature [6–8], polyHIPE nanocomposites also offer an effective solution for the removal of organic pollutants as polymer-based adsorbents, thanks to their well-defined macroporous structure. Physical and morphological properties of polyHIPEs can be easily tuned by controlling experimental parameters during emulsion preparation [3, 9, 10]. Morphological properties of polyHIPEs dependent are strongly on the primary HIPEs. Thereby, emulsion stabilization is a key factor of producing polyHIPEs with well-defined pore structures [11]. Primary HIPE templates can be prepared via surfactant stabilization or particle stabilization. When particle stabilization is used resulting HIPEs are often named as Pickering-HIPEs [12]. Particle stabilization provides additional benefits based on the structure and property of the particulates. Moreover, this approach avoids the disadvantages arise from the use excessive amount of surfactants [12]. Particles can give functionality to polyHIPEs (i.e. magnetism, electrical conductivity, etc.), act as filler or reinforcement or bring additional sites to participate in crosslinking [11, 12]. For instance, cellulose nanocrystals can be used for Pickering-emulsion stabilization due to their amphiphilic nature and ability to adsorb at the oil/water interface or water/oil interface [13–17]. In this respect, particle stabilization can be used as a tool for preparing polyHIPEs nanocomposites [18].

HIPEs can be polymerized by applying different polymerization approaches including free radical polymerization, controlled radical polymerization, ring opening polymerization (ROP), condensation polymerization and ring opening metathesis polymerization (ROMP), based on the chemical structure of polymerizable unit(s) in the continuous emulsion phase [11]. In this manner, not only chemical functionality but also morphological and mechanical properties of polyHIPEs can be altered by changing the monomer chemistry. For instance, low-mechanical strength resulted from highly porous structure can be avoided by using monomers that give tough and durable polymer networks. ROMP of dicyclopentadiene (DCPD) has tremendous contribution on the preparation of polyHIPEs with remarkable mechanical properties [19–23]. On the other hand, unsaturated bonds on polyDCPD main chains create a disadvantage by causing susceptibility to oxidation [19, 21], while also providing suitable sites for functionalization. Oxidation problem can be solved by converting double bonds by modification [19]. Another solution can be delaying oxidation process by using antioxidants [24].

Cellulose nanocrystals (CNC) are precursor materials which are easily functionalized has an increasing research potential in recent years about developing efficient adsorbent materials for treatment of wastewater. Since CNC is non-toxic, low cost, biodegradable, renewable, easy to modification and biocompatible feedstock, many different modification methods were reported in literature until today for functionalization of CNC and the designing of efficient CNC-based adsorbents with the aim of removal of contaminants from aqueous media. In this respect, Oyewo et. al developed sawdust-derived CNC coagulant for the removal of Cd and Ni from water. Modification of CNC by $NaNO_2$/$NaHCO_3$ highly efficient removal of Ni and Cd was achieved [25]. Xi et al. synthesized different adsorbents based on crosslinking action between CNC and polyethyleneimine (PEI) in presence of iron ions as bridge joint and investigated performance of adsorbents in the arsenic removal [26]. The nanocellulose based pH-sensitive nanoparticles were also synthesized and used for treatment of As (V) pollution in acidic aqueous environment [27]. As (III) removal from wastewater by manganese-based CNC/PEI as a new adsorbent was also studied and arsenic removal efficiency was reported [28]. In another study, Köse et. al reported CNC modified glycidyl methacrylate based cryogels for methyl orange adsorption and demonstrated that modification of cryogels by CNC remarkably improved swelling properties and influenced dye adsorption capacity [29].

In our previous contribution, we studied preparation of polystyrene-based functionalized cellulose nanocrystal (fCNC) reinforced polyHIPEs for the improvement of morphological, mechanical, and thermal properties of polyHIPEs [30]. For this purpose, we used 3-methacryloxypropyltrimethoxysilane to functionalize CNC and prepared surfactant stabilized HIPEs containing fCNCs. More recently, we used unmodified CNCs to prepare polystyrene-based polyHIPE adsorbents and achieved a maximum adsorption capacity of 70% for Nile blue using monoliths containing 9 wt% CNC [31]. Herein, we described preparation of polyHIPE/CNC nanocomposites from ROMP of the surface-modified CNC stabilized DCPD-based Pickering-HIPEs. Surface modification treatments during the preparation of polymer nanocomposites or functionalization of nanostructures can be conducted for different goals such as improving the interfacial adhesion, enhancing the performance, and etc. [32, 33]. In order to improve the compatibility of CNC with emulsion phases and increase the hydrophobicity, we used epoxy-terminated PEG for the surface modification of CNC. Furthermore, we demonstrated the influence of emulsion structure and emulsification on the properties of polyHIPEs nanocomposites by using response surface design methodology based on statistical analysis. Finally, we used statistical analysis results to select an adsorbent material from among resulting polyHIPE/CNC nanocomposites. Consequently, we revealed adsorptive properties of selected nanocomposite by testing Nile blue adsorption from aqueous solutions.

Experimental

Materials

Poly(ethylene glycol) methyl ether (average Mn ~ 2000, Sigma-Aldrich), epichlorohydrin (for synthesis, Sigma-Aldrich), boron trifluoride-methanol solution (50% w/w in methanol, Sigma-Aldrich), dichloromethane (anhydrous, ≥ 99.8%, contains 40–150 ppm amylene as stabilizer, Sigma-Aldrich), sodium hyrdroxide (reagent grade, ≥ 98%, pellets (anhydrous), Sigma-Aldrich), (3-aminopropyl) trimethoxysilane (97%, Sigma-Aldrich), dicyclopentadiene (contains BHT as stabilizer, Sigma-Aldrich), octadecyl 3-(3,5-di-tert-butyl-4-hydroxyphenyl)propionate (99%, Sigma-Aldrich), Pluronic® L121 (poly(ethylene glycol)-block-poly(propylene glycol)-block-poly(ethylene glycol), average Mn ~ 4,400, Sigma-Aldrich), Grubbs Catalyst® M204 (Umicore, Sigma-Aldrich) were all purchased from Sigma-Aldrich and used as received. Cellulose nanocrystal (Dia: 10–20 nm, L: 300–900 nm) was purchased from Nanografi (Ankara, Turkey). Ethanol was technical grade and used without purification. In all experiments ultrapure deionized water was used.

Preparation of PEG-m-CNCs

PEG-m-CNCs were prepared in 3-steps. In the first step monofunctional epoxy-terminated poly(ethylene glycol) (Epoxy-PEG) was first synthesized. For this purpose, 5.0 g of poly(ethylene glycol) methyl ether and 0.2313 g (2.5 mmol) of epichlorohydrin were placed into a 2-neck reactor equipped with a condenser. Then the reactor was immersed in an oil bath and placed on a magnetic stirrer. When the temperature was fixed at 55 °C, 1.0 mL of boron trifluoride-methanol solution was added into the reactor and stirring (@700 rpm) was continued for 4 h. The reactor was then removed from the oil bath and wait to cool down. When the temperature dropped to 25 °C, 0.1 g of NaOH was added into the mixture and the mixture was stirred for 24 h at a constant speed of 700 rpm. After 24 h, 80 mL of dichloromethane was added on the mixture and then the product was separated by precipitation in diethyl ether and dried in a vacuum oven for 24 h at room temperature.

In the second step, (3-aminopropyl) trimethoxysilane (APTMS) was grafted on CNCs. In this respect, 10 mL of APTMS, 80 mL of ethanol, 20 mL of ultrapure deionized water and 2.0 g of CNCs were mixed in a 250 mL flask, on a magnetic stirrer at a constant speed of 250 rpm for 5 h at room temperature. Then, the product was filtered using a vacuum system and dried in a vacuum oven at 40 °C for 24 h. The obtained particles were kept at 110 °C for 2 h for self-crosslinking over the silane groups. Afterwards, particles were extracted with ethanol for 24 h and the resulting APTMS grafted CNCs (APTMS@CNCs) were dried in a vacuum oven at 40 °C for 24 h.

In the third step PEG-m-CNCs was obtained by the reaction between Epoxy-PEG and APTMS@CNCs. With this aim, 1.0 g of APTMS@CNCs was dispersed in 50 mL of ultrapure deionized water at a constant stirring rate of 700 rpm in a two-necked reactor equipped with a condenser. Then the reactor was placed in oil bath on a magnetic stirrer and the temperature a-was set to 65 °C. The mixture was stirred 30 min at constant temperature. Afterwards, 0.5 g of Epoxy-PEG was added into the mixture and stirring was continued for 24 h. Afterwards the mixture was dialyzed against deionized water for 2 days. It was then transferred to a beaker and covered by aluminum foil. The beaker was placed in a freezer and kept at − 40 °C for 2 h. In the end frozen mixture was freeze-dried for 48 h to obtain PEG-m-CNCs.

Synthesis of PolyDCPC/CNC PolyHIPE Nanocomposites

For the preparation of precursor HIPE templates 4 experimental parameters, namely the amount of PEG-m-CNCs loading, emulsifier amount, internal phase ratio, and stirring rate were selected as the main parameters that determine properties and three distinctive levels (low [− 1], medium [0], and high [+ 1]) were assigned for each of them (Table 1). The other parameters were all kept constant during the experiments. To synthesize polyDCPC/CNC polyHIPE nanocomposites, precursor HIPE formulation were created according to the experimental design matrix presented in Table 2.

In a typical experiment DCPD, PEG-m-CNCs, emulsifier (Pluronic L®121) and antioxidant (octadecyl 3-(3,5-di-tert-butyl-4-hydroxyphenyl)propionate) (0.2 wt% regarding to DCPD) were placed in a two-necked round-bottom reactor equipped with an overhead stirrer. Then the reactor was immersed in an oil bath and placed on a hot-plate fixed at a constant temperature (@25 °C). Then constant stirring (@400 rpm) was applied until a homogeneous mixture of the components was obtained. Afterwards, internal phase was added dropwise at a constant pumping rate (@50 rpm) by using a peristaltic pump, and under constant stirring. Once the addition of internal phase completed stirring was continued for an extra 1 h, then Grubbs Catalyst® M204 (1 mol% regarding to DCPD) was added after dissolving in 1 mL of toluene. Thereafter, resulting HIPEs were quickly transferred into cylindrical glass bottles and kept at 80 °C in an air circulating oven for 3 h in order to achieve crosslinking.

Table 1 Levels of factors

Factors	Experimental parameters	Levels		
		Low [− 1]	Medium [0]	High [1]
A				
X_1	Emulsifier amount (vol%, with regards to continuous phase volume)	3	4	5
B				
X_2	Amount of PEG-m-CNCs Loading (wt%, with regards total monomer composition)	0.50	0.75	1.00
C				
X_3	Internal phase ratio (vol%, with regards total emulsion volume)	75	80	85
D				
X_4	Stirring rate (rpm)	500	1000	1500

Table 2 Experimental design matrix

Std order No.	Center Pt	Blocks	Factors			
			A	B	C	D
1	1	1	− 1	− 1	− 1	− 1
2	1	1	1	− 1	− 1	− 1
3	1	1	− 1	1	− 1	− 1
4	1	1	1	1	− 1	− 1
5	1	1	− 1	− 1	1	− 1
6	1	1	1	− 1	1	− 1
7	1	1	− 1	1	1	− 1
8	1	1	1	1	1	− 1
9	1	1	− 1	− 1	− 1	1
10	1	1	1	− 1	− 1	1
11	1	1	− 1	1	− 1	1
12	1	1	1	1	− 1	1
13	1	1	− 1	− 1	1	1
14	1	1	1	− 1	1	1
15	1	1	− 1	1	1	1
16	1	1	1	1	1	1
17	0	1	0	0	0	0
18	0	1	0	0	0	0
19	0	1	0	0	0	0
20	0	1	0	0	0	0

Resulting polyHIPE nanocomposites were Soxhlet-extracted with ethanol for 24 h, and then dried under vacuum at 25 °C until constant weight is available. A schematic illustration for Pickering-HIPE preparation and Pickering-polyHIPE synthesis is presented in Fig. 1. All samples were stored in inert atmosphere to avoid oxidation. By varying formulations according to the experimental design matrix 20 different samples were prepared. PolyHIPE nanocomposites were named as x-CP, where x is designating the number of Std Order. The samples synthesized according to the Std Order No between 17 and 20 are the control samples having identical formulations. Thereby, variation of the data obtained for these samples reflects the error caused by the experimenter.

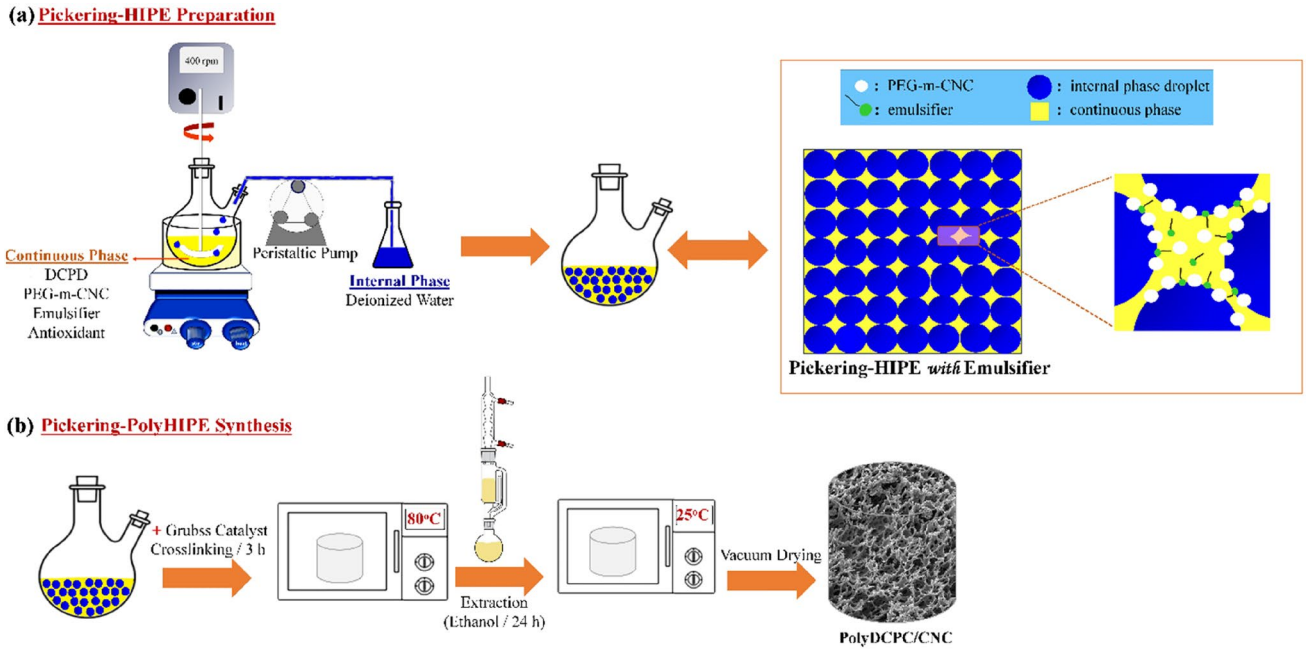

Fig. 1 Schematic representation of Pickering-HIPE preparation (**a**) and DCPD-based Pickering-polyHIPE synthesis (**b**)

Characterization

Functional CNCs

Fourier Transform Infrared (FTIR) spectroscopy was conducted by using Bruker ALPHA FT-IR spectrometer with a Platinum ATR. X-ray diffraction analysis was performed by using Malvern Panalytical Empyrean High Temperature X-Ray Diffractometer (HT-XRD).

Thermogravimetric analysis (TGA) was conducted by using Seiko TG/DTA 6300 thermal analysis equipment (Seiko instruments Inc., Tokyo, Japan). TGA thermograms were recorded under inert atmosphere at a heating rate of 10 °C min^{-1} between 30 and 650 °C.

Scanning Electron Microscopy (SEM) images were recorded by using FEI Quanta FEG 250. Transmission Electron Microscopy (TEM) was recorded by using Hitachi HT-7700 microscope equipped with lanthanum hexaboride (LaB6) electron gun at Eastern Anatolia High Technology Application and Research Center (DAYTAM).

PolyDCPC/CNC PolyHIPE Nanocomposites

Morphological properties of polyHIPE nanocomposites were investigated by SEM (ZEISS Supra 40 VP). For this purpose, samples were all coated with gold pre-analysis. SEM images at different magnifications were recorded and used for the calculation of average cavity diameters (R1) and interconnected pore diameters (R2). For this purpose, at least 100 measurements were taken from each sample and corrected with a factor before calculating R1 and R2 [9, 10].

Gas adsorption/desorption was used to determine specific surface area (R3) of the samples. In this respect, Brunauer–Emmet–Teller (BET) equation was applied to N_2 adsorption/desorption isotherms of each sample. Samples were prepared to analysis by applying a degassing procedure using Micromeritics FlowPrep 060 Sample Degas System (Micromeritics Instrument Corporation, USA). Degassing procedure was conducted for 24 h at room temperature. Afterwards, adsorption/desorption isotherms were recorded on a Micromeritics Gemini VII VII 2390t Overall Automatic Surface Area and Porosity Analyzer (Micromeritics Instrument Corporation, USA). Skeletal density (R4) and average pore volume (R5) of the samples was determined by using a Helium gas pycnometer cell (Micromeritics AccuPyc II 1340 V1.05). Prior to analysis, samples were first left at atmospheric conditions for 5 days and then powdered in liquid nitrogen by using an analytical mill (IKA/A 10 basic).

Foam densities (R6) of the samples were calculated according to Archimedes' principle by using an analytical balance equipped with a density determination kit (Weightlab WSA224T). For the determination of R3, R4, R5 and R6, measurements were repeated 3 times for each sample by using different specimens and the arithmetic average value of three measurements was calculated for each property.

Compression moduli (R7) of the samples were tested on a ZwickRoell Z020 Universal Testing Machine (Zwick GmbH & Co. KG, Germany) equipped with a 10 kN load cell. Uniaxial compression tests were applied according to ASTM

D1621 (Standard Test Method for Compressive Properties of Rigid Cellular Plastics) by using geometrically identical samples of 25 mm in diameter and 10 mm in height. For each sample, tests were repeated 5 times using 5 different specimens. R7 was calculated from the initial slope of the stress–strain plots, which were drawn by using the original data obtained from the testXpert II Testing Software (Zwick GmbH & Co. KG, Germany). For each sample, the average value of R7 was calculated by taking the arithmetic average of compression modulus data recorded by five different measurements.

Statistical Analysis

Statistical analysis of the experimental results was conducted by using Minitab® 21.1© 2021 (Minitab, LLC) Statistical Software for Windows. For this purpose, the data obtained by material characterization were tabulated in the order of design matrix presented in Table 2. Accordingly, original data obtained from the Minitab® 21.1 software was used for statistical analysis. In Table 2, the column of "Center Pt" demonstrates experimental runs where factor levels are set in the center of the low and high settings. In here, "1" symbolizes the corner point while "0" represent a center point. In addition, the column of "Blocks" demonstrates the grouped together experimental runs which are obtained under similar conditions.

Adsorption Experiments

Nile blue adsorption was tested by carrying out ultraviolet/visible measurements. For this purpose, batch adsorption experiments were conducted in 250 mL Erlenmeyer flasks. In order to reveal the influence of pH, experiments were first repeated at different pH values ranging between 2.0 and 9.0 by using stock solutions with an initial dye concentration of 10 mg L^{-1}. For this purpose, adsorbents were immersed in 150 mL of dye solution after setting pH values by using 0.1 M HCl or 0.1 M NaOH. Afterwards, flasks were placed on an IKA Ks 130 Basic S1 Orbital Shaker at 300 rpm at 25 °C, and shaked until equilibrium was reached. The influence of initial dye concentration was studied at pH 4 and under similar experimental conditions by changing the concentration of Nile blue between 30 and 120 mg L^{-1}. In order to calculate the sorption efficiency and adsorption capacity, the change of dye concentration in the solutions was periodically measured (λ_{max} = 635 nm) by using a T80 + UV–VIS spectrophotometer (PG Instruments Ltd). The equilibrium concentration of Nile blue (q_e) and sorption efficiency (SE %) were calculated according to the following equations, where C_o and C_t (mg/L) are respectively Nile blue concentrations at t = 0 and t in the solution, V (L) is the volume of the solution and m (g) is the weight of adsorbent:

$$q_e = \left[\frac{(C_o - C_t)}{C_o}\right] \times (V/m) \quad (1)$$

$$SE\% = \left[\frac{(C_o - C_t)}{C_o}\right] \times 100 \quad (2)$$

Results and Discussion

Functional CNCs

Successful synthesis of PEG-m-CNCs was confirmed by FT-IR spectroscopy. For this purpose, comparative FT-IR spectra of APTMS@CNCs, Epoxy-PEG and PEG-m-CNCs are presented in Fig. 2. When the characteristic peaks of CNCs are examined (Fig. 2a), the wide peak observed in the range of 3000–3600 cm^{-1} is due to the stretching vibrations of the O–H groups of cellulose and the peak appeared at 2872 cm^{-1} is due to the C-H bonds. The peaks arise at 1321 and 1416 cm^{-1} are due to the CH_2 and CH bendings, respectively. However, the peaks observed at around 1160 cm^{-1} and 1110 cm^{-1} can be attributed to the C–O–C asymmetric vibrations [34]. In the spectrum of APTMS@CNCs presented in Fig. 2b, the low-intensity peak observed at 1585 cm^{-1} is due to bending vibrations of the NH_2 groups and demonstrates successful grafting of APTMS groups onto CNC surface [35, 36]. In Fig. 2c, the broad band in the range of 3400–3600 cm^{-1} can be attributed to O–H bonds. The peaks observed at 2883 cm^{-1} and 1464 cm^{-1} are respectively originated from the CH and CH_2 groups, while the peaks at

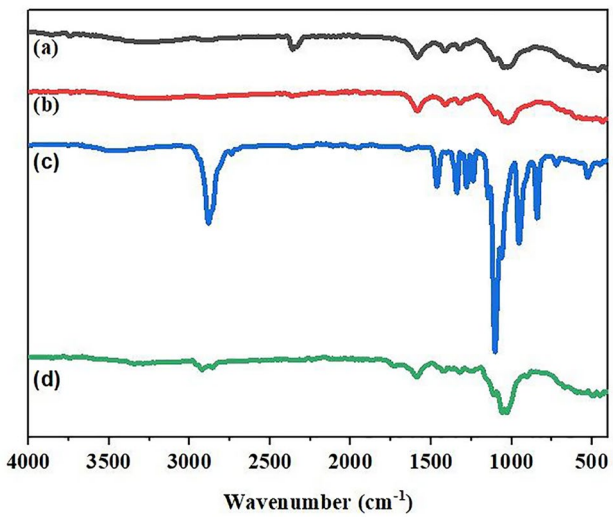

Fig. 2 Comparative FTIR spectra of (a) CNCs, (b) APTMS@CNCs, (c) Epoxy-PEG, and (d) PEG-m-CNCs

1341 cm^{-1} and 1103 cm^{-1} are due to the C–O groups [37]. In addition, the peak appeared at 954 cm^{-1} can be attributed to the terminal epoxy group. In the spectrum of PEG-m-CNCs (Fig. 2d), the disappearance of the epoxy peak at 954 cm^{-1}, indicates the successful grafting of Epoxy-PEG onto the APTMS@CNCs surface.

The peaks observed at 17°, 23° and 34.2° in the XRD patterns of the unmodified CNCs (Fig. 3) are for the typical cellulose (101), (002) and (040) crystallographic planes, respectively [30]. The peaks at 17° and 23° are also appeared in the XRD pattern of PEG-m-CNC with lower intensities, whereas the peak at 34.2° was considerably diminished most probably due to the destruction and decrystallization by surface functionalization.

According to TGA thermograms presented in Fig. 4 both unmodified and modified CNCs exhibited similar decomposition profiles. The first stage of decomposition was continued up to about 100 °C and can be attributed to the removal of water from the structure. Secondary mass loss was observed in the range of ~ 100–250 °C and it was followed by the massive mass loss between 250 and 350 °C. It can be concluded from the TGA curves that Epoxy-PEG modified CNCs (PEG-m-CNC) exhibits a more intense mass loss compared to the bare CNCs. This result can be attributed to the degradation of surface grafted organic groups on the CNC surfaces. In the final stage of thermal degradation, the differences between the degradation rate and the amount of mass loss became more significant. TGA analysis revealed that while bare CNCs lost 61.6% of its total mass up to 650 °C, PEG-m-CNCs lost 69.5%. The difference of 7.9 wt% might be correlated to the polymer groups grafted on the CNC surfaces.

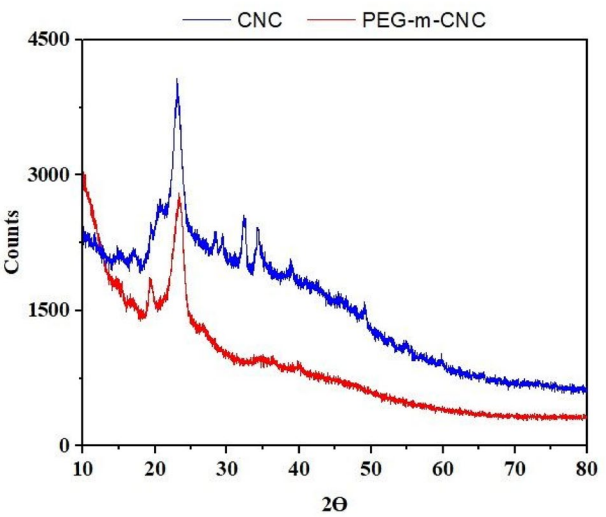

Fig. 3 XRD spectra diffractograms of CNCs and PEG-m-CNCs

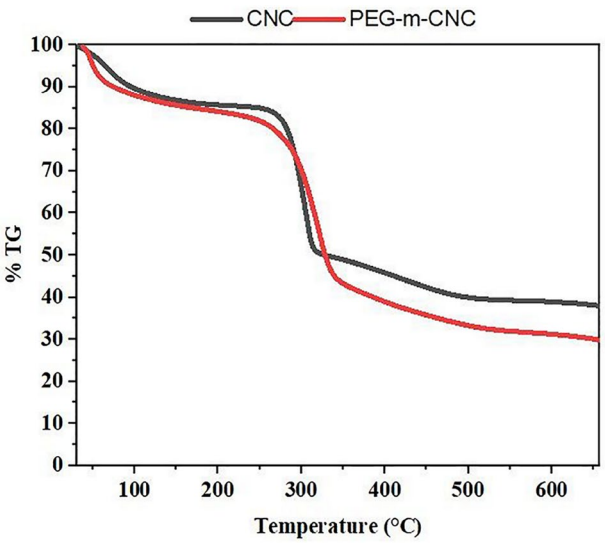

Fig. 4 Comparative TGA thermograms of CNCs and PEG-m-CNCs

The comparison of the SEM images of unmodified CNCs and PEG-m-CNCs presented in Fig. 5 demonstrates that the surface of CNC is completely covered by Epoxy-PEG. This result is also supported by the TEM analysis. The comparative TEM images of unmodified CNCs and modified CNCs presented in Fig. 6 confirmed that surface modification of CNC with Epoxy-PEG remarkably improved the dispersity of nanoparticles.

PolyDCPC/CNC PolyHIPE Nanocomposites

PolyDCPC/CNC polyHIPE nanocomposites were synthesized according to the experimental design matrix presented in Table 2 by using the 3 different levels of experimental parameters given in Table 1. Consequently, 20 different polyHIPE nanocomposite samples produced with internal phase ratios changing between 75 and 85 vol%, and PEG-m-CNC loading of 0.50, 0.75, or 1.0 wt%. Pore morphology of the polyHIPE nanocomposites were investigated by SEM and presented in Figure S1. It can be seen from the images given in Figure S1 that despite Pickering-polyHIPEs usually exhibits limited openness [11, 12]; all resulting samples have an open porous morphology. Moreover, there is no evidence of emulsion destabilization processes were occurred due to nanoparticle loading during polymerization. This is probably due to the surface grafted epoxy-terminated PEG groups increasing the compatibility of modified CNCs [30]. However, spherical cavities were deformed in some cases. This deformation was a result of highly rigid structure of the CNC supported polyDCPD matrix. Since the obtained materials showed significantly high strength it was very difficult to prepare samples for SEM imaging, even in liquid nitrogen. The deformation observed in the SEM images is due to the

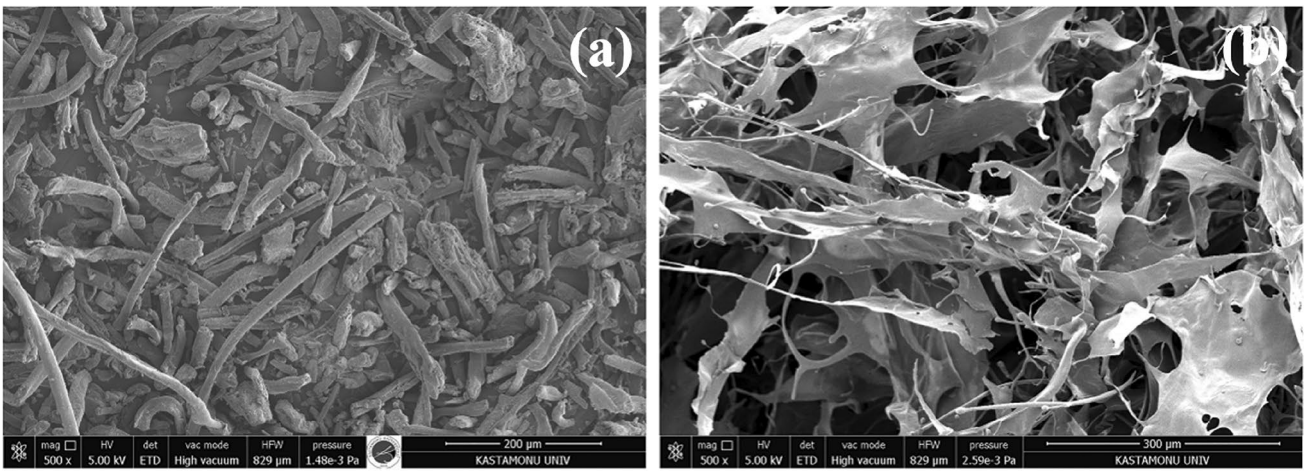

Fig. 5 SEM images of **a** unmodified CNCs and **b** PEG-m-CNCs

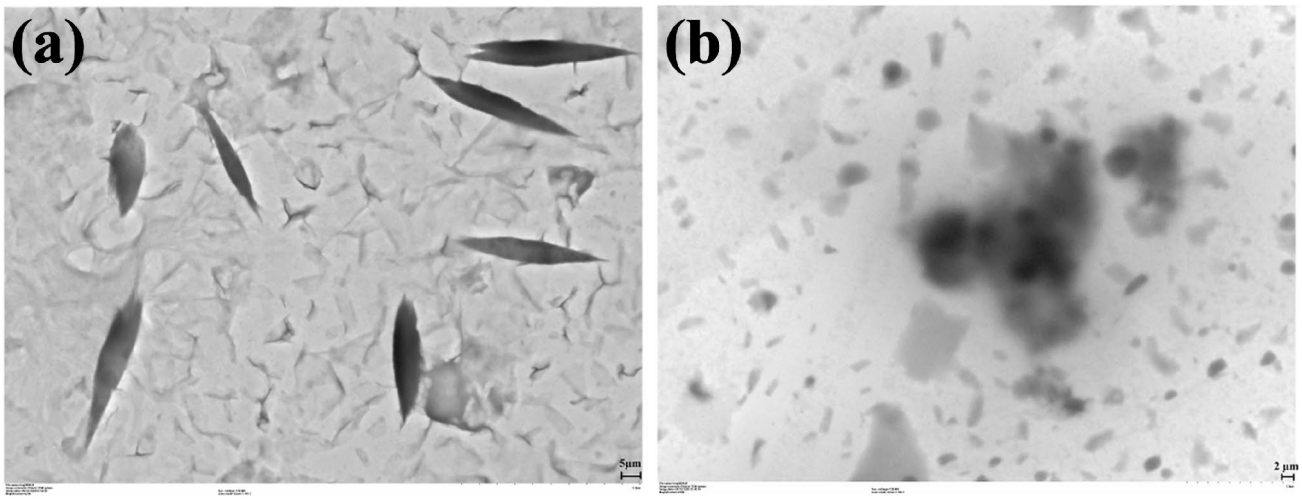

Fig. 6 TEM images of **a** unmodified CNCs and **b** PEG-m-CNCs

elongation of cavity walls in the direction of the applied force while trying to break the samples. The morphological and physical properties of the samples are presented in Table 3, where the characterization data were tabulated. Average cavity diameters (R1) of the polyHIPE nanocomposites were found to be change between 4.85 and 14.52 µm, interconnected pores (R2) were between 1.75 and 5.34 µm. The control samples (Std Order No 17-20) have relatively close cavity and pore sizes suggesting that the samples were synthesized with a good coherence and accuracy. BET specific surface areas (R3) of the polyHIPE nanocomposites were ranged between 2.27 $m^2 g^{-1}$ and 8.01 $m^2 g^{-1}$ (Table 3), while the control samples exhibited BET specific surface areas ranged between 3.92 and 4.26 $m^2 g^{-1}$. Table 3 also reveals that the skeletal densities, foam densities, and pore volumes were also varied according to the variation of the precursor HIPE template formulations. Once again, these values were all determined to be altered in a good coherence for the control samples.

Mechanical properties of the polyHIPE nanocomposites were investigated in terms of compressive properties by applying uniaxial force. Compressive stress–strain plots were drawn for each sample and presented in Figure S2, while compression modulus data (Table 3) were determined from the slope of the curves using the original software of the test equipment. For each polyHIPE nanocomposite, stress–strain plots were all similar and have both the linear shear stress–strain region and plastic deformation region. This result is suggesting that all samples follow similar deformation model under compressive load. However, compression moduli of the polyHIPE nanocomposites were found to be altered between 7.2 and 62 MPa, whereas

Table 3 Characterization data for the polyHIPE nanocomposites

Std order No.	Sample code	R1 (μm)	R2 (μm)	R3 ($m^2\ g^{-1}$)	R4 ($g\ cm^{-3}$)	R5 (cm^3)	R6 ($g\ cm^{-3}$)	R7 (MPa)
1	1-CP	12.66	5.34	2.50	1.10	0.97	0.36	59.0
2	2-CP	14.52	3.88	2.27	1.09	0.93	0.35	58.3
3	3-CP	7.90	2.63	2.92	1.08	0.91	0.38	54.0
4	4-CP	4.85	2.37	3.07	1.08	1.02	0.40	62.0
5	5-CP	7.71	3.80	4.14	1.08	0.68	0.32	17.2
6	6-CP	6.84	4.03	5.30	1.09	0.75	0.25	7.2
7	7-CP	7.97	4.65	4.26	1.12	0.63	0.26	18.8
8	8-CP	8.47	4.09	5.03	1.07	0.71	0.26	9.3
9	9-CP	6.64	2.47	3.65	1.08	1.03	0.35	48.0
10	10-CP	7.94	3.96	4.72	1.08	1.07	0.40	38.3
11	11-CP	7.20	2.62	3.86	1.07	1.10	0.37	17.6
12	12-CP	5.10	1.75	6.03	1.09	1.09	0.37	26.7
13	13-CP	5.95	3.07	5.60	1.09	0.78	0.26	8.7
14	14-CP	5.94	3.22	7.24	1.11	0.68	0.29	12.1
15	15-CP	6.82	4.49	5.43	1.08	0.73	0.26	15.3
16	16-CP	6.93	2.56	8.01	1.06	0.73	0.28	9.6
17	17-CP	9.10	4.23	3.92	1.06	0.87	0.37	30.4
18	18-CP	6.71	4.27	3.97	1.07	0.88	0.28	25.0
19	19-CP	6.59	4.08	4.26	1.05	0.97	0.28	27.0
20	20-CP	7.55	5.15	4.21	1.11	0.93	0.31	24.0

R1—average cavity diameter, R2—average interconnected pore diameter, R3—BET specific surface area, R4—skeletal density, R5—pore volume, R6—foam density, R7—compression modulus

the control samples have moduli changing between 24 and 30 MPa. The large difference in compression modulus of polyHIPE nanocomposites can be attributed to the variation of experimental parameters. However, it should be noted that the polyDCPD matrix is very prone to oxidation and different levels of oxidation of the samples cause different degrees of reduction in mechanical properties [22, 24].

Statistical Analysis

The influence of the variation of experimental parameters presented in Table 1 (emulsifier amount, A; the amount of PEG-m-CNCs loading, B; internal phase ratio, C; stirring rate, D) on average cavity size (R1), interconnected pore size (R2), BET specific surface area (R3), pore volume (R4), skeletal density (R5), foam density (R6), and compression modulus (R7) were investigated with statistical approach. The main and interaction effects of experimental parameters were determined by using Minitab® 21.1© 2021 (Minitab, LLC) Statistical Software for Windows with a confidence level of 95% ($\alpha = 0.05$). The effects of control factors on the selected responses (R1–R7) were expressed via model mathematical equations based on the response surface design approach as given in Eq. 3. In Eq. 3 β_0 and β_i are respectively the global mean and the regression coefficients corresponding to main effects and interactions, whereas CtPt is corresponding to the center points. The model equations for R1-R7 are presented in Eqs. 4–10. The regression coefficients associated standard errors, t and p-values for each response are presented in Tables S1–S7, R-sq and R-sq(adj) values are given in Tables S8–S14 in the Supplementary Material File. In addition, F ratios and p-values determined by analysis of variance (ANOVA) are also presented in Tables S8–S14. The magnitude of the main effects and interactions of the experimental factors on the responses (R1-R7) was also determined by conducting Student t-test. Pareto-charts for each response are presented in Fig. 7. In these charts the t-value is expressed by red dashed line for a 95% confidence level and states the statistical significance of the main effects and interaction effects on the studied response. If a given horizontal column in a Pareto chart is above the t-value, the corresponding interaction can be expressed as statistically significant.

$$\begin{aligned} R = {} & \beta_0 + \beta_1 A + \beta_2 B + \beta_3 C + \beta_4 D + \beta_5 A * B \\ & + \beta_6 A \times C + \beta_7 A \times D + \beta_8 B \times C + \beta_9 B \times D \\ & + \beta_{10} C \times D + \beta_{11} A \times B \times C + \beta_{12} A \times B \times D \\ & + \beta_{13} A \times C \times D + \beta_{14} B \times C \times D \\ & + \beta_{15} A \times B \times C \times D + \beta_{16} CtPt \end{aligned} \quad (3)$$

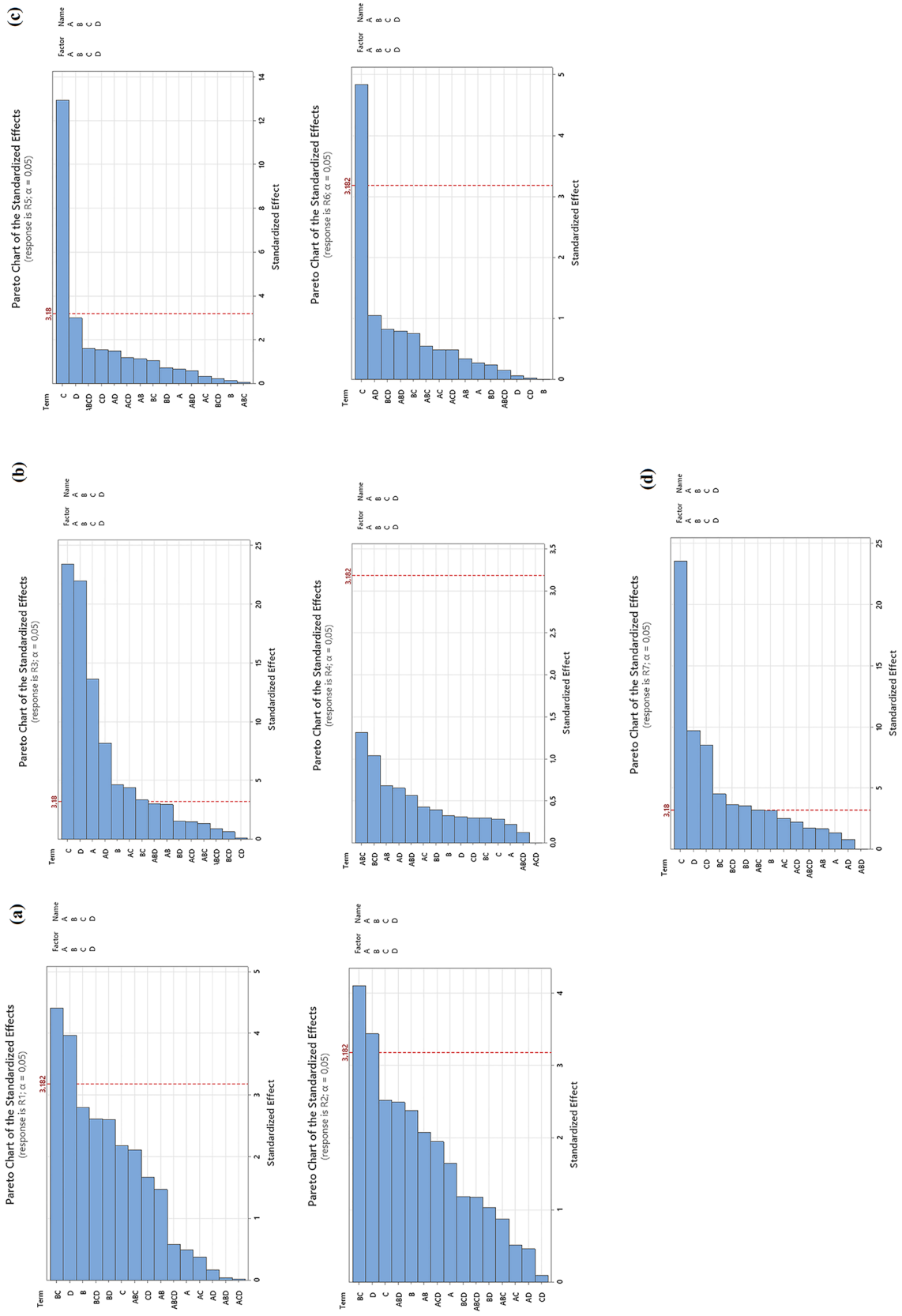

Fig. 7 Pareto charts of the standardized effects: **a** R1 and R2; **b** R3 and R4; **c** R5 and R6; **d** R7

$$\begin{aligned} R1 =& 7.714 - 0.145\,A - 0.813\,B - 0.634\,C - 1.151\,D \\ & - 0.427\,A\times B + 0.109\,A\times C + 0.051\,A\times D + 1.280\,B\times C \\ & + 0.755\,B\times D + 0.485\,C\times D + 0.614\,A\times B\times C \\ & + 0.013\,A\times B\times D + 0.006\,A\times C\times D - 0.759\,B\times C\times D \\ & - 0.171\,A\times B\times C\times D - 0.224\,Ct\,Pt \end{aligned} \quad (4)$$

$$\begin{aligned} R2 =& 3.436 - 0.200\,A - 0.289\,B + 0.306\,C - 0.417\,D \\ & - 0.252\,A\times B - 0.063\,A\times C + 0.056\,A\times D \\ & + 0.498\,B\times C + 0.125\,B\times D + 0.012\,C\times D \\ & - 0.106\,A\times B\times C - 0.302\,A\times B\times D - 0.236\,A\times C\times D \\ & - 0.144\,B\times C\times D + 0.143\,A\times B\times C\times D + 0.995\,Ct\,Pt \end{aligned} \quad (5)$$

$$\begin{aligned} R3 =& 4.6295 + 0.5817\,A + 0.1985\,B + 1.0001\,C \\ & + 0.9396\,D + 0.1266\,A\times B + 0.1871\,A\times C \\ & + 0.3497\,A\times D - 0.1429\,B\times C \\ & + 0.0665\,B\times D + 0.0047\,C\times D \\ & - 0.0585\,A\times B\times C + 0.1296\,A\times B\times D \\ & - 0.0641\,A\times C\times D + 0.0275\,B\times C\times D \\ & + 0.0382\,A\times B\times C\times D - 0.5347\,Ct\,Pt \end{aligned} \quad (6)$$

$$\begin{aligned} R4 =& 1.08770 - 0.00139\,A - 0.00204\,B + 0.00177\,C \\ & - 0.00196\,D - 0.00425\,A\times B - 0.00266\,A\times C \\ & + 0.00407\,A\times D - 0.00186\,B\times C - 0.00247\,B\times D \\ & + 0.00186\,C\times D - 0.00822\,A\times B\times C \\ & + 0.00354\,A\times B\times D + 0.00000\,A\times C\times D \\ & - 0.00650\,B\times C\times D + 0.00081\,A\times B\times C\times D \\ & - 0.0123\,Ct\,Pt \end{aligned} \quad (7)$$

$$\begin{aligned} R5 =& 0.8658 + 0.0078\,A + 0.0017\,B - 0.1518\,C + 0.0352\,D \\ & + 0.0132\,A\times B - 0.0040\,A\times C - 0.0175\,A\times D \\ & - 0.0125\,B\times C + 0.0086\,B\times D - 0.0182\,C\times D \\ & + 0.0007\,A\times B\times C - 0.0070\,A\times B\times D \\ & - 0.0141\,A\times C\times D + 0.0029\,B\times C\times D \\ & + 0.0188\,A\times B\times C\times D + 0.0464\,Ct\,Pt \end{aligned} \quad (8)$$

$$\begin{aligned} R6 =& 0.3262 + 0.0027\,A - 0.0001\,B - 0.0489\,C - 0.0006\,D \\ & + 0.0035\,A\times B - 0.0050\,A\times C + 0.0106\,A\times D \\ & - 0.0077\,B\times C - 0.0025\,B\times D - 0.0003\,C\times D \\ & + 0.0055\,A\times B\times C - 0.0080\,A\times B\times D \\ & + 0.0050\,A\times C\times D + 0.0083\,B\times C\times D \\ & - 0.0016\,A\times B\times C\times D - 0.0137\,Ct\,Pt \end{aligned} \quad (9)$$

$$\begin{aligned} R7 =& 28.881 - 0.944\,A - 2.219\,B - 16.606\,C - 6.844\,D \\ & + 1.181\,A\times B - 1.781\,A\times C + 0.581\,A\times D \\ & + 3.194\,B\times C - 2.519\,B\times D + 5.994\,C\times D \\ & - 2.256\,A\times B\times C + 0.031\,A\times B\times D \\ & + 1.569\,A\times C\times D + 2.569\,B\times C\times D \\ & - 1.231\,A\times B\times C\times D - 2.28\,Ct\,Pt \end{aligned} \quad (10)$$

R1 model equation (Eq. 4) reveals that the main interactions of experimental parameters have a reverse contribution on the determination of average cavity diameter. Based on the regression coefficients, the order of the influence of main effects can be written as: D > B > C > A. Since resulting polyHIPE nanocomposites were all produced from Pickering-HIPE templates, this result demonstrates the importance of stabilizing ability of the used nanoparticles and their homogeneous distribution in the precursor emulsions. It is well-known that the cavity size and cavity size distribution of polyHIPEs are related to emulsion stability. The increase in cavity diameter indicates lower emulsion stability [11]. According to R1 model equation, the increase in stirring rate and nanoparticle loading decreases the average cavity diameter, which shows that smaller emulsion droplets are formed while emulsion stability is increased. The influence of nanoparticle loading on the variation of average cavity diameters can be discussed by comparing previous findings obtained by statistical modelling of polyHIPEs. For instance, in our previous study we have reported that internal phase ratio was the most important factor on the determination of average cavity diameter of polyHIPEs produced from surfactant stabilized HIPEs [9]. However, our more recent work on nanoclay incorporated polyHIPE nanocomposites produced from surfactant stabilized HIPEs showed the influence of nanoparticle loading on average cavity diameter. It was determined that internal phase ratio is less determinative as compared to stirring duration, emulsifier amount and nanoclay loading [10]. While this result can be attributed to the stability behavior of emulsion templates in the presence of nanoparticles, our new findings are in good agreement with this. As can be seen from the R1 model equation, not only the main effects but duo and trio interactions are also important for the variation of average cavity size. The order of the most significant interaction effects can be written according to regression coefficients as: B × C > B × C × D > B × D > A × B × C > C × D > A × B. However, the Pareto chart of R1 response presented in Fig. 7a demonstrates that the binary effect B × C and main effect D have statistical

significance. As well as B, B × C × D and B × D are close to t-value which is minimum statistically significant influence magnitude, they do not have statistical significance due to below this magnitude.

R2 model equation (Eq. 5) reveals that other than internal phase ratio, main effects of experimental parameters have a decreasing influence on interconnected pore diameter. Which can be also stated as the internal phase ratio increases interconnected pore diameter of the produced polyHIPE nanocomposites increases. Considering the regression coefficients in Eq. 5, the magnitude of the main effects can be ranged as: D > C > B > A. On the other hand, as the interaction effects of experimental factors are also examined, the alignment of regression coefficients in R2 model equation emphasize that the most significant contribution on the determination of interconnected pore diameter is the binary interaction of the amount of PEG-m-CNCs loading and internal phase ratio (B × C). This is followed by the main effect of the stirring rate. Pareto chart of R2 (Fig. 7a) is confirming that D and B × C have statistical significance. This result might be ascribed to the nature of Pickering-HIPEs and it is consistent with R1 model equation given in Eq. 4.

The relation of BET specific surface area of polyHIPE nanocomposites is expressed by the R3 model equation (Eq. 6), which shows positive contribution of main effects on this property. While the magnitude of the main effects can be aligned as C > D > A > B, dual interactions of the selected parameters also have remarkable importance. Moreover, Pareto chart of R3 response (Fig. 7b) reveals that C, D, A, B main effects and A × D, A × C, B × C binary interactions have statistically significant contribution on the BET specific surface area. This result shows that the internal phase ratio has an important role, both alone and in combination with other parameters, and as well as the importance of synergistic interactions between experimental parameters. However, it also contradicts our previous findings, which reveals that internal phase ratio has no meaningful effect on the BET surface area of polyHIPE produced from surfactant stabilized HIPEs.

The dependence of skeletal density to experimental parameters was also investigated statistically and R4 model equation (Eq. 7) was derived. However, the R-sq and R-sq(adj) values of R4 equation was respectively found to be 65.4% and 0.0% (Table S14). This can be interpreted as this equation is not statistically significant. In addition, Pareto chart of R4 response presented in Fig. 7b also demonstrates that none of the main effects or interaction effects has statistical significance. We believe that this result is due to the highly oxidized polymer matrix. Since polyDCPD based polyHIPE nanocomposites exhibit high strength, freshly synthesized unoxidized samples could not be powdered. For this reason, skeletal densities were measured by using oxidized samples. As it is well-known, oxidative degradation leads to chemical structure changes in polymers, it also causes formation of scratches and fine cracks on the surface. In addition, polymer molecular weight can be decreased or increased due to the breakage of molecular chains or by cross-linking and/or chain branching. All of these structural alterations change physical and mechanical properties of polymeric materials (i.e. reduced flexibility, impact resistance, and breaking strain, discoloration, etc.) [38]. Most probably, skeletal densities of the polyHIPE nanocomposites were varied due to the oxidation degree of the specimens, which cannot be controlled.

When the regression coefficients of R5 model equation presented in Eq. 8 and Pareto chart of R5 response (Fig. 7c) examined, it can be stated that only the main effect of internal phase ratio has statistical significance on the determination of pore volume. Since it has a negative coefficient, the increase of internal phase ratio would lead a decrease in the pore volumes of nanocomposites. Because pores of a polyHIPE are reflecting emulsion droplets, this result is consistent with the suggested theories about the pore formation of polyHIPEs [11] and consistent with previously published results [10].

It can be seen from the regression coefficients of Eq. 9 and Pareto chart of R6 (Fig. 7c) that the main effect of internal phase ratio is the only parameter which has statistical significance on the determination of foam density. Increasing the internal phase ratio decreases the foam density, as expected. According to R7 model equation (Eq. 10), compression modulus is strongly dependent on both main effects and interaction effects of experimental parameters. In this respect, the magnitude of the main effects can be aligned as C > D > B > A, while duo and trio interactions can be ranged as C × D > B × C > B × C × D > B × D > A × B × C > A × C × D and > A × B × C × D. However, Pareto chart of R7 response given in Fig. 7d demonstrates that A, A × C, A × C × D and A × B × C × D has no statistical significance. Moreover, main effects have a negative influence on the compression modulus. Comparison of the regression coefficients shows that increasing internal phase ratio remarkable decreases R7. This can be attributed to the increased overall porosity of the produced polyHIPE nanocomposites. Increasing nanoparticle loading leads decrease in compression modulus, on the contrary of expectations. However, synergistic interactions between the amount of PEG-m-CNCs loading and other experimental parameters, namely internal phase ratio, stirring rate and emulsifier amount, appear to be quite important.

Adsorption Properties

Ionization degree of the ions in the solution and surface charge of the adsorbents are known to be strongly influenced by the pH of the solutions. Since the adsorption equilibrium

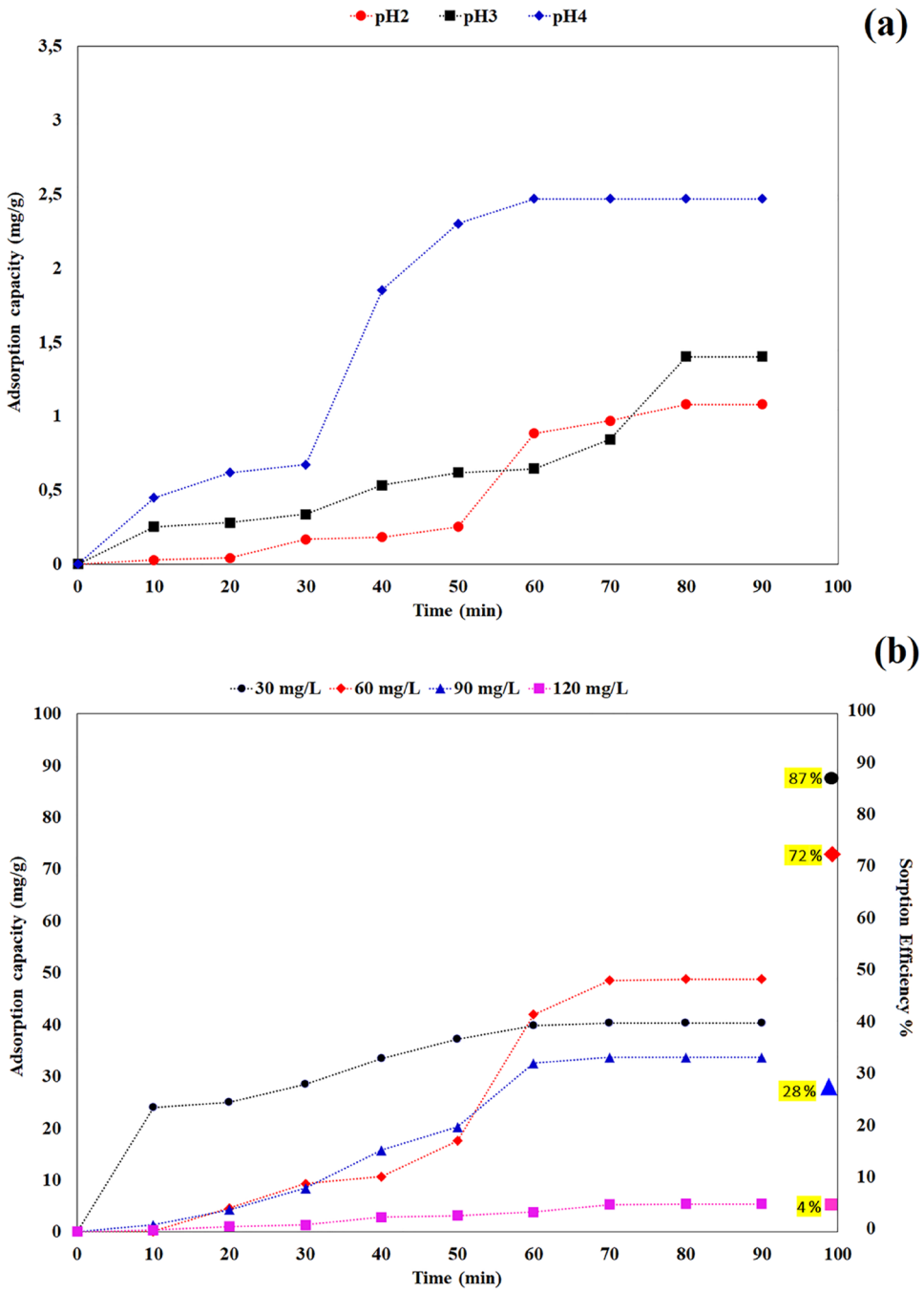

Fig. 8 Influence of **a** pH and **b** initial dye concentration on adsorption capacity and sorption efficiency

can be changed due to the dissociation of functional groups on the adsorbent surface, pH of the solutions is an important parameter in terms of adsorption efficiency [39]. In this study, when the pH of the aqueous dye solutions was higher than 4.0, the color of the solutions turned from blue to pink/purple and precipitation occurred, most probably due to the change of ionization degree. Thereby, influence of pH was studied at pH = 2.0, 3.0, and 4.0. Figure 8a demonstrates that adsorption of Nile blue was increased with the increasing pH. This result can be attributed to stronger electrostatic interactions between the negatively charged anionic dye and the adsorbent surface due to the increase in the positive charge density on the adsorbent surface.

Dependence of adsorption capacity and sorption efficiency of polyHIPE/CNC adsorbent on initial Nile blue concentration is shown in Fig. 8b. When the initial concentration of dye increased, both adsorption capacity and sorption efficiency were decreased significantly. This result can be ascribed to the adsorbate-adsorbent interactions. At lower dye concentrations adsorbate molecules can easily interact with the available active sites and adsorption proceeded more rapidly with a high efficiency. However, at higher dye

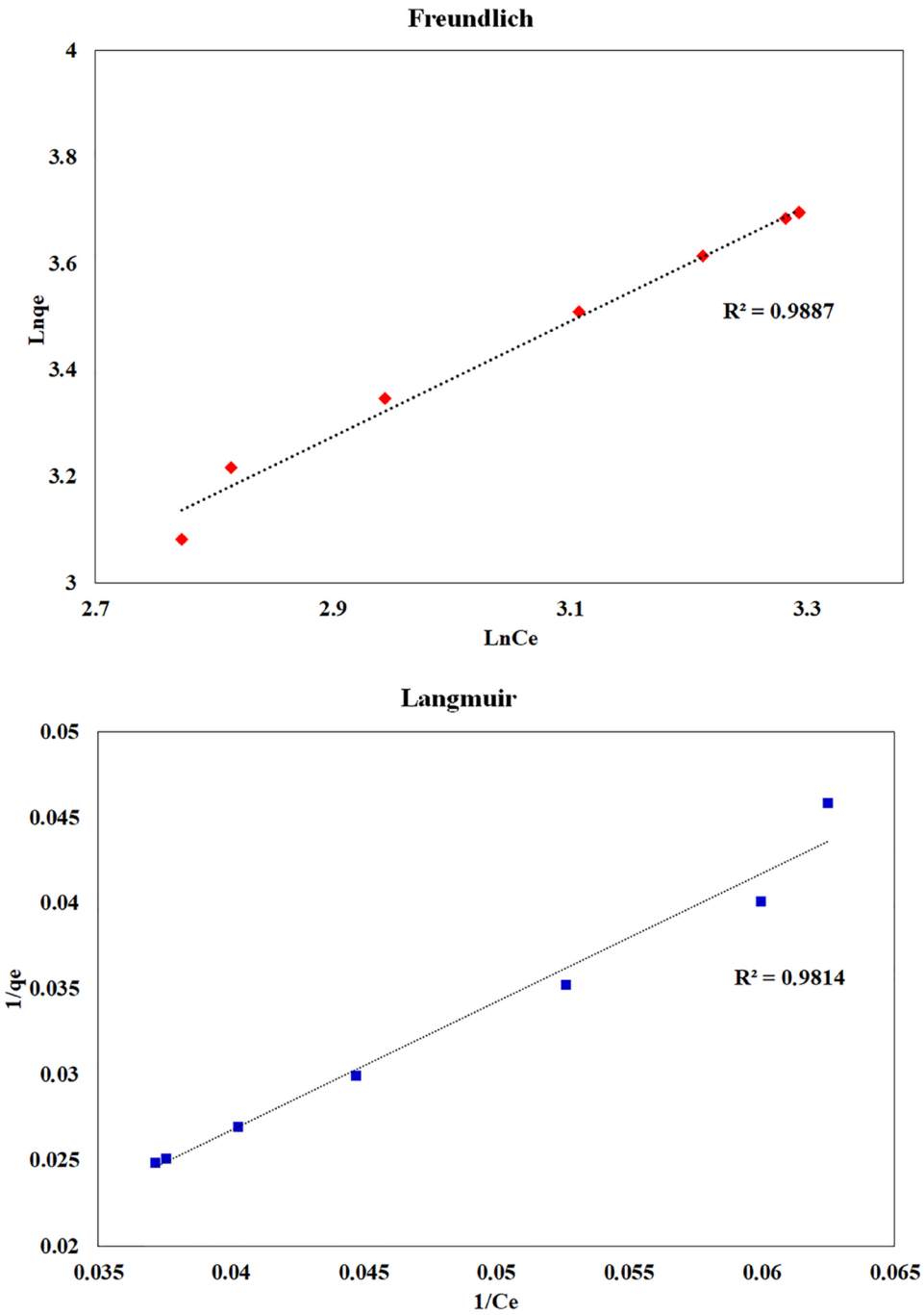

Fig. 9 The Freundlich and Langmuir isotherm plots of Nile blue adsorption on polyHIPEs/CNC monolith

concentrations, in addition to the increased repulsive forces in between, adsorbate molecules also required to compete to interact with active sites on the adsorbent surface. Herein, the highest sorption efficiency was obtained for the system studied at a fixed initial dye concentration of 30 mg L^{-1} (87%).

Adsorption Isotherms

The equilibrium of adsorption was investigated by employing Langmuir and Freundlich equations to experimental data. The Langmuir isotherm expressed by Eq. 11, assumes that the adsorption phenomenon is monolayer, whereas Freundlich isotherm given by Eq. 12 is applicable for heterogeneous surface energy systems.

Table 4 Calculated parameters for adsorption isotherms and kinetic models

Adsorption isotherms		Kinetic models	
Langmuir model		Pseudo first-order	
q_{max} (mg g^{-1})	303.03	q_e (mg g^{-1})	2.45
K_L (L mg^{-1})	4.39×10^{-3}	k_1 (min^{-1})	3.66×10^{-2}
r^2_L	0.9814	r^2_1	0.7688
Freundlich model		Pseudo second-order	
K_F (mg g^{-1})	1.13	q_e (mg g^{-1})	4.97
n	0.92	k_2 (g mg^{-1} min^{-1})	1.22×10^{-2}
r^2_F	0.9887	r^2_2	0.9618

$$\frac{1}{q_e} = \left(\frac{1}{q_{max} K_L}\right)\frac{1}{C_e} + \frac{1}{q_{max}} \tag{11}$$

$$\mathrm{Ln}\, q_e = \mathrm{Ln}\, K_f + \frac{1}{n}\mathrm{Ln}\, C_e \tag{12}$$

In the given equations below, q_e (mg g^{-1}) and C_e (mg L^{-1}) are respectively the equilibrium Nile blue concentration on the adsorbent and in solution, and q_{max} (mg g^{-1}) is the monolayer capacity of the adsorbent. K_L (L mg^{-1}) is the Langmuir constant, while K_F (mg g^{-1}) is the Freundlich constant. n is a dimensionless heterogeneity factor indicating the nature of the adsorption process. It is dependent on the surface heterogeneity. When $n < 1$, it is assumed that the process is physical and when $n = 1$ or $n > 1$, it is chemical and linear in nature [31].

By fitting the experimental data to Eqs. 11 and 12, Langmuir and Freundlich isotherms were obtained for Nile blue adsorption on polyHIPEs/CNC adsorbent (Fig. 9). The parameters calculated for adsorption isotherms are listed in Table 4. The applicability of the adsorption isotherms can be seen from the correlation coefficients (Table 4) and linear relationship of isotherms (Fig. 9). In both cases the degree of linearity is very high, though regression coefficient of Freundlich isotherm plot is slightly higher than that of the Langmuir plot. This infers that both Freundlich and Langmuir models can be used to understand adsorption properties; however, Freundlich isotherm was the best fitted model. The n value obtained from Freundlich isotherm was found to be 0.92 (Table 4) indicates that the adsorption is a chemical process [40]. The affinity between the sorbate molecules and the adsorbent can be predicted by using a dimensionless Langmuir separation factor, R_L. R_L can be calculated by using the equation presented in Eq. 13, where K_L is the Langmuir constant and C_o is the initial concentration.

$$R_L = \frac{1}{\left(1 + K_L C_o\right)} \tag{13}$$

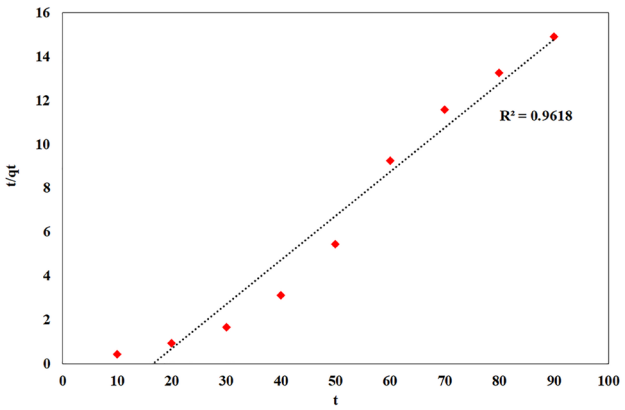

Fig. 10 Pseudo second-order kinetics of Nile blue adsorption on polyHIPEs/CNC monolith

When $R_L = 0$ the isotherm is assumed to be irreversible, whereas it is linear if $R_L = 1$. If the value of R_L varies between 0 and 1 ($0 < R_L < 1$) it is favorable, and unfavorable if it is greater than 1 ($R_L > 1$) [40]. Herein, R_L was calculated to be 0.83, suggesting that the adsorption is favorable.

Adsorption Kinetics

Kinetic mechanism of Nile blue adsorption on polyHIPE/CNC adsorbent was investigated by fitting experimental data to pseudo first-order and pseudo first-order rate equations presented respectively in Eqs. 14 and 15. In the given equations q_e and q_t (mg g^{-1}) are the amounts of Nile blue adsorbed at equilibrium and at time t, k_1 (min^{-1}) and k_2 (g mg^{-1} min^{-1}) are the pseudo first-order and pseudo second-order rate constants, respectively.

$$\mathrm{Ln}\left(q_e - q_t\right) = \mathrm{Ln}\, q_e - k_1 t \tag{14}$$

$$\frac{t}{q_t} = \frac{1}{k_2 q_e^2} + \frac{1}{q_e t} \quad (15)$$

When the experimental data were fitted to Eqs. 14 and 15, adsorption capacities and rate constants were determined from the straight-line plots of pseudo first-order (not shown here) and pseudo second-order (Fig. 10) kinetic models as listed in Table 4. As can be seen the correlation coefficients of the straight-line plots for the pseudo first-order (r^2_1) and pseudo second-order kinetic model (r^2_2) were determined to be 0.7688 and 0.9618, respectively. Based on this finding, it can be considered that adsorption follows pseudo second-order kinetic model and chemisorption is the rate-limiting adsorption type. This result can be evaluated as adsorption was controlled by the interactions between the active sites on the adsorbent surface and sorbate molecules [31]. PEG-m-CNC nanoparticles have abundant of oxygen atoms, which increases the hydrophilicity of the adsorbent surface and improves the applicability of the adsorbent in aqueous environment [41]. The additional functionality provided with PEG-*m*-CNC loading to the polyDCPD based monolithic adsorbents plays a significant role in adsorption. Nile blue is strongly interacted with adsorbent and deposited on the surface via π–π interactions.

Conclusion

In this study, polyDCPD-based polyHIPE/CNC nanocomposites were developed by using experimental design approach. PolyDCPD is known by distinctive mechanical properties and its suitability for post-functionalization through unsaturated bonds. On the other hand, CNCs are sustainable materials that can improve material properties and introduce functionality for further applications such as developing efficient adsorbents for wastewater treatment. Herein, surface modified CNCs were used in emulsion stabilization to prepare Pickering-HIPEs and produce polyHIPE nanocomposites. Moreover, the influences of experimental parameters on the morphological and physical properties were determined via statistical analysis to develop an approach for material design. In the end seven different mathematical model equations were derived to express the relation between the experimental parameters and final material properties. By using these equations, a polyHIPE/CNC nanocomposite was selected as model adsorbent and implemented in the removal of Nile blue dye from aqueous solutions. It was found that sorption efficiency for polyHIPE/CNC adsorbent was 87%. It was also shown that both Freundlich and Langmuir models can be used to explain the adsorption process and the adsorption kinetics fit the pseudo-second-order kinetic model. The n value obtained from Freundlich isotherm was found to be 0.92 that remarks chemical adsorption. The Langmuir separation factor, R_L was found to be 0.83, indicating that the adsorption is favorable. The pseudo second-order kinetic model (r^2_2) was calculated to be 0.9618. As a result, it was demonstrated that the developed polyHIPE/CNC composites are prospective adsorbents for applications such as treatment of contaminated aqueous media thanks to further functionality provided with PEG-m-CNC loading to the polyDCPD-based macroporous polymer foams.

Supplementary Information The online version contains supplementary material available at https://doi.org/10.1007/s10924-022-02549-4.

Funding This study was supported by the Scientific and Technological Research Council of Turkey (TÜBİTAK; Project No: 119N705), Ministry of Science, Research and Technology of Iran (MSRT; Project No: 99-24-800). Authors thank to TÜBİTAK, MSRT and University of Tabriz for financing this project.

Data Availability The data that support the findings of this study are available from the authors, upon reasonable request.

Declarations

Conflict of interest The authors have not disclosed any competing interests.

References

1. Silverstein MS (2014) Polymer 55:304–320
2. Lissant KJ (1966) J Colloid Interface Sci 22:462–468
3. Foudazi R (2021) React Func Polym 164:104917
4. Sajad S, Moghbeli MR (2020) React Func Polym 146:104406
5. Moghbeli MR, Khajeh A, Alikhani M (2017) Chem Eng J 309:552–562
6. Han N, Wang S, Yao Z, Zhang W, Zhang X, Zeng L, Chen R (2020) EcoMat 2:e12044
7. Han N, Yao Z, Ye H, Zhang C, Liang P, Sun H, Wang S, Liu S (2019) Sustain Mater Tech 17:e00108
8. Wang S, Zhang W, Jia F, Fu H, Liu T, Zhang X, Liu B, Núñez-Delgado A, Han N (2021) J Environ Manage 292:112763
9. Mert HH, Mert MS, Mert EH (2019) Mater Res Express 6:115306
10. Mert EH, Mert HH (2021) Polym Compos 42:724–738
11. Mert HH, Mert EH (2022) Advanced functional porous materials. In: Uthaman A, Thomas S, Li T, Maria H (eds) Engineering materials, 1st edn. Springer, Cham
12. Zhang T, Sanguramath RA, Israel S, Silverstein MS (2019) Macromolecules 52:5445–5479
13. Marinova KG, Alargova RG, Denkov ND, Velev OD, Petsev DN, Ivanov IB, Borwankar RP (1996) Langmuir 12:2045–2051
14. Kalashnikova I, Bizot H, Cathala B, Capron I (2011) Langmuir 27:7471–7479
15. Capron I, Rojas OJ, Bordes R (2017) Curr Opin Colloid Interf Sci 29:83–95
16. Fujisawa S, Togawa E, Kuroda K (2017) Sci Technol Adv Mater 18:959–971
17. Varanasi S, Henzel L, Mendoza L, Prathapan R, Batchelor W, Tabor R, Garnier G (2018) Front Chem 6:409

18. Dupont H, Fouché C, Dourges MA, Schmitt V, Héroguez V (2020) Carbohydr Polym 243:116411
19. Kovačič S, Krajnc P, Slugovc C (2010) Chem Commun 46:7504–7506
20. Kovačič S, Jeřábek K, Krajnc P, Slugovc C (2012) Polym Chem 3:325–328
21. Mert EH, Slugovc C, Krajnc P (2015) Express Polym Lett 9:344–353
22. Yüce E, Mert EH, Krajnc P, Parın FN, San N, Kaya D, Yıldırım H (2017) Macromol Mater Eng 302:1700091
23. Kovačič S, Slugovc C (2020) Mater Chem Front 4:2235–2255
24. Yüce E, Krajnc P, Mert HH, Mert EH (2019) J Appl Polym Sci 136:46913
25. Oyewo OA, Mutesse B, Leswifi TY, Onyango MS (2019) J Environ Chem Eng 7:103251
26. Xi C, Wang R, Rao P, Zhang W, Yan L, Li G, Chai F, Cai Y, Luo T, Zhou X (2020) Carbohydr Polym 237:116129
27. Chai F, Wang R, Yan L, Li G, Cai Y, Xi C (2020) Carbohydr Polym 245:116511
28. Luo T, Wang R, Chai F, Jiang L, Rao P, Yan L, Hu X, Zhang W, Wei L, Khatee A, Han N (2022) Chemosphere 303:134925
29. Köse K, Mavlan M, Nuruddin M, Gómez AMU, Youngblood JP (2022) Cellulose 29:1623–1636
30. Mert HH, Moghbeli MR, Sajad S, Mert EH (2020) React Func Polym 151:104572
31. Eslek A, Kekevi B, Mert HH, Mert EH (2022) J Appl Polym Sci 139:51802
32. Han N, Zhao X, Thakur VK (2021). Nano Mater Sci. https://doi.org/10.1016/j.nanoms.2021.11.004
33. Han N, Liu P, Jiang J, Ai L, Shao Z, Liu S (2018) J Mater Chem A 6:19912
34. Rafieian F, Jonoobi M, Yu Q (2019) Cellulose 26:3359–3373
35. Jonoobia M, Ashorib A, Siracusa V (2019) Polym Test 76:333–339
36. Lee HG, Kim GH, Ha CS (2017) Mater Today Commun 13:275
37. Yin Y, Ma J, Tian X, Jiang X, Wang H, Gao W (2018) Cellulose 25:6447–6463
38. Izdebska J (2016) 22 – In: Izdebska J, Thomas S. (eds) Printing on Polymers, 1st edn. William Andrew Publishing.
39. Nisar A, Bibi I, Said A, Nawaz S, Ali Z, Salman SM, Iqbal HMN, Bilal M (2020) Case Stud Chem Environ Eng 2:100040
40. Ajenifuja E, Ajao JA, Ajayi EOB (2017) Appl Water Sci 7:2279–2286
41. Abbasi S, Noorizadeh H (2017) Carbon Lett 23:30–37